BNL-211424-2019-JAAM

Isothermal Microcalorimetry: Insight into the Impact of Crystallite Size and Agglomeration on the Lithiation of Magnetite, Fe3O4

M. M. Huie, E. S. Takeuchi

To be published in "ACS APPLIED MATERIALS & INTERFACES"

February 2019

Energy Sciences Directorate

Brookhaven National Laboratory

U.S. Department of Energy

USDOE Office of Science (SC), Basic Energy Sciences (BES) (SC-22)

Notice: This manuscript has been authored by employees of Brookhaven Science Associates, LLC under Contract No. DE-SC0012704 with the U.S. Department of Energy. The publisher by accepting the manuscript for publication acknowledges that the United States Government retains a non-exclusive, paid-up, irrevocable, world-wide license to publish or reproduce the published form of this manuscript, or allow others to do so, for United States Government purposes.

DISCLAIMER

This report was prepared as an account of work sponsored by an agency of the United States Government. Neither the United States Government nor any agency thereof, nor any of their employees, nor any of their contractors, subcontractors, or their employees, makes any warranty, express or implied, or assumes any legal liability or responsibility for the accuracy, completeness, or any third party's use or the results of such use of any information, apparatus, product, or process disclosed, or represents that its use would not infringe privately owned rights. Reference herein to any specific commercial product, process, or service by trade name, trademark, manufacturer, or otherwise, does not necessarily constitute or imply its endorsement, recommendation, or favoring by the United States Government or any agency thereof or its contractors or subcontractors. The views and opinions of authors expressed herein do not necessarily state or reflect those of the United States Government or any agency thereof.

Isothermal Microcalorimetry: Insight into the Impact of Crystallite Size and Agglomeration on the Lithiation of Magnetite, Fe_3O_4

*Matthew M. Huie[a‡], David C. Bock[b‡], Andrea M. Bruck[c], Killian R. Tallman[a], Lisa M. Housel[a], Lei Wang[c], Juergen Thieme[d], Kenneth J. Takeuchi[a,c], Esther S. Takeuchi[a, b, c], Amy C. Marschilok[a, b, c]**

[a] Department of Materials Science and Chemical Engineering, Stony Brook University, Stony Brook, NY 11794, USA

[b] Energy and Photon Sciences Directorate, Brookhaven National Laboratory, Upton, NY 11973 USA

[c] Department of Chemistry, Stony Brook University, Stony Brook, NY 11794, USA

[d] National Synchrotron Light Source II, Brookhaven National Laboratory, Upton, NY 11973 USA

*corresponding author: amy.marschilok@stonybrook.edu

‡ these authors contributed equally to the manuscript

Abstract

Magnetite, Fe_3O_4, holds significant interest as a Li-ion anode material because of its high theoretical capacity (926 mAh/g) associated with multiple electron transfers per cation center.

Notably, both crystallite size and agglomeration influence ion transport. This report probes the effects of crystallite size (12 and 29 nm) and agglomeration on the reactions involved with the formation of the surface electrolyte interphase on Fe_3O_4. Isothermal microcalorimetry (IMC) was used to determine the parasitic heat evolved during lithiation by considering the total heat measured, cell polarization, and entropic contributions. Interestingly, the 29 nm Fe_3O_4 based electrodes produced more parasitic heat than the 12 nm samples (1346 J/g vs. 1155 J/g). This observation was explored using scanning electron microscopy (SEM) and X-ray fluorescence mapping in conjunction with spatially resolved x-ray absorption spectroscopy (XAS). SEM imaging of the electrodes revealed more agglomerates for the 12 nm material, affirmed by XRF maps. Further, XAS results suggest Li^+ transport is more restricted for the smaller crystallite size (12 nm) material, attributed to its greater degree of agglomeration. These results rationalize the IMC data, where agglomerates of the 12 nm material limit SEI formation and parasitic heat generation during lithiation of Fe_3O_4.

1. Introduction

The transition metal oxide magnetite, Fe_3O_4, is attractive as a next generation anode material for Li-ion batteries as it offers low cost, low toxicity and a high specific capacity (924 mAh/g) resulting from the ability to transfer multiple electrons per cation center.[1-2] Fe_3O_4 adopts an inverse spinel oxide structure with a close packed oxygen framework and iron ions occupying tetrahedral (8a) and octahedral (16d) sites.[3] Due to the dense crystallographic structure of the material, poor Li^+ and Fe^{2+}/Fe^{3+} mobility can cause significant overpotentials[4] that limit full electrochemical utilization of the material, particularly at higher current densities.[5] To mitigate

overpotential in Fe_3O_4, a common strategy is to nanosize the active material, thereby reducing the length of solid-state diffusion pathways and increasing active surface area.[2, 6-7] The approach has been effective in improving rate capability and increasing utilization of the material.[8-9]

One consequence of nanosizing Fe_3O_4 is that the resulting small crystallites may undergo significant agglomeration, which is apparent when the active material is processed into a composite electrode.[10] TEM imaging of Fe_3O_4 electrodes indicate that the resulting agglomerates consist of tightly packed crystallites with low void space. [10] Depending on the size of the agglomerate and the packing of individual crystallites, active material utilization can be reduced for crystallites located towards the center of the aggregate at high (de)lithiation rates. Multi-scale mathematical models, which account for mass transport at both crystallite and agglomerate length scales, indicate that the relative importance of transport limitations at these two length scales is dependent on the size of the primary crystallites.[11-12] For Fe_3O_4 crystallites < 10 nm in size, the models indicate that transport limitations through the agglomerate are the critical factor, but for larger crystals (ca. 30 nm), transport through both crystallites and agglomerates are significant [11-12] Thus, consideration of Li ion transport through both crystallites and formed agglomerates of Fe_3O_4 is critical for assessing electrochemical behavior.

In addition to size and morphology, the electrochemical function of Fe_3O_4 is impacted by the formation of the electrically insulating solid electrolyte interphase layer (SEI) on the active material particles. [13-15] Ideally, the SEI, once formed, protects the active material from further reaction with the electrolyte while still allowing the transport of Li^+ ions during subsequent electrochemical cycling. Yet, for conversion electrode materials such as Fe_3O_4, which undergo large volume changes during lithiation and delithiation, each cycle presents the possibility of exposing new surface area for additional electrolyte reduction.[16-17] Continual formation of

additional SEI consumes lithium ions, solvent and can also insulate particles electrically, resulting in electrochemical isolation of the active material and subsequent capacity fading.[16, 18-19]

Direct characterization of the SEI layer is challenging because it is a thin (<100 nm), amorphous layer composed of light elements (Li, C, O, F) and is sensitive to air and moisture. In a recent report, the chemical composition of SEI formed on Fe_3O_4 was investigated through XPS.[13] In ethylene carbonate based electrolyte, it was found that the SEI consisted primarily of lithium carbonate, lithium alkyl carbonates, lithium alkoxide, and lithium fluoride components. These compounds are also primary components of the SEI formed on graphite[20-23], and thus the SEI composition is anticipated to be similar for Fe_3O_4 and conventional graphite based anodes.

A relatively under-reported technique for analyzing the onset of electrolyte reduction associated with SEI formation and the heat that it generates is isothermal microcalorimetry (IMC). IMC has been used to study parasitic heat flows[24-28] and the effects of electrolyte additives[26, 29] in the formation of the SEI layer on graphite anodes.[30-31] In a recent study, IMC was used to characterize SEI in Fe_3O_4 based electrodes, representing the first use of the technique for studying a conversion electrode material.[32] Heat flow during the first lithiation of Fe_3O_4 was measured with IMC and was compared with heat contributions predicted from heats of formation for the Faradaic reaction, cell polarization, and entropic contributions.[32] The difference between total heat flow observed and the sum of polarization and entropic contributions was attributed to heat evolved from non-Faradaic (parasitic) side reactions associated with SEI formation. *Operando* X-ray absorption near edge structure (XANES) spectroscopy was used to track oxidation state as a function of lithiation via linear combination fitting of the data to reference spectra. The results showed that between ~ 1.9 and 2.7 electron

equivalents of lithiation, the average Fe oxidation state remained constant at approximately +2, while from 0 – 1.9 electron equivalents and from 2.7 – 8.3 electron equivalents the Fe oxidation state reduced linearly with measured electrochemical electron transfer. These results provide evidence that the reduction of electrolyte and onset of SEI formation was the primary electrochemical reaction between 1.9 and 2.7 electron equivalents during the lithiation of Fe_3O_4. The XANES result was in good agreement with the microcalorimetry data, which indicated deviation of measured heat flow from values predicted by polarization and entropic contributions beginning at approximately 2 electron equivalents.

For the first time, we explore the role of crystallite size on non-faradaic heat generation associated with SEI formation in Fe_3O_4 electrodes, while also considering the impact of crystallite agglomeration. Using Fe_3O_4 synthesized at both 12 nm and 29 nm, IMC was used to investigate the thermodynamic behavior during the first lithiation process. Both SEM and XRF imaging of the electrodes revealed more aggregates for the 12 nm material. *Operando*, micron resolution x-ray absorption near edge structure (XANES) measurements were used to determine the lithiated phase composition across agglomerates at multiple discharge rates. The complimentary SEM, XRF, and spatially resolved XANES measurements provide a mechanistic basis for the seemingly counterintuitive result of reduced parasitic heat flow in 12 nm vs. 29 nm Fe_3O_4 electrodes, where closely packed crystallites in agglomerates of the 12 nm crystallites reduce electrolyte access and limit the amount of SEI formed during lithiation.

2. Experimental

2.1 Synthesis of 12 nm and 29 nm Fe_3O_4

Fe_3O_4 of 12 nm and 29 nm crystallite size was synthesized using previously reported co-precipitation methods. [6-7, 33] Briefly, for the synthesis of 12 nm Fe_3O_4, an aqueous solution of $FeCl_2 \cdot 4H_2O$ was added dropwise to a deoxygenated mixture of NH_4OH and H_2O. [6-7, 33] The product was washed with water until neutral and then vacuum dried. For the synthesis of 29 nm Fe_3O_4 an aqueous solution of $FeCl_2 \cdot 4H_2O$ was dropped into a deoxygenated mixture NH_4OH and H_2O and stirred under air for 24 hours. The product was washed with water until neutral and dried under vacuum.

2.2 Physical Characterization of Fe_3O_4

X-ray powder diffraction data was collected using a Rigaku Miniflex X-ray diffractometer with a Cu Kα source. Crystallite sizes for Fe_3O_4 were determined from Rietveld refinement using GSAS-II software and a structural model of Fe_3O_4 (PDF #01-088-0315). R_{wp} values from the Rietveld fits were < 2.0%. Scanning electron microscopy (SEM) measurements were collected with an analytical high-resolution SEM (JEOL 7600F) instrument, operating at an accelerating voltage range of 10 kV. Surface area of the Fe_3O_4 powders was determined through nitrogen gas adsorption using the Brunauer-Emmett-Teller (BET) method. BET measurements were conducted using an 11 point analysis with a Quantachrome Nova 4200e.

2.3 Electrochemistry for Thermal Measurements

Electrodes were prepared using a slurry of 80 wt% Fe_3O_4 and 20 wt% polyvinylidene fluoride (PVDF) in N-methyl-2-pyrrolidone (NMP) cast onto copper foil. Coin type cells were assembled with lithium metal anodes, polypropylene separators and an electrolyte of 1 M $LiPF_6$ in ethylene carbonate (EC): dimethyl carbonate (DMC) 30:70 by volume.

2.3.1 Isothermal Microcalorimetry (IMC)

Coin cells were wired and placed in the ampoules of a TA instruments TAM III microcalorimeter and held at a constant temperature of 30 °C. The cells were discharged and the heat dissipation was measured against a reference ampoule. Lithiation was performed with a Bio-logic VSP potentiostat at a constant current rate of 40 mA/g (C/25) to 0.03 V. After lithiation, the cells rested at open circuit voltage for 24 hours.

2.3.2 Open-circuit Potential (OCP) and Calculation of Contributions from Entropic Heat (ΔS) and Polarization Heat

Coin cells were used to measure open-circuit potentials (OCPs) at various depths of discharge (DOD) during lithiation of Fe_3O_4. The cells were discharged in short segments of time in an environmental chamber kept at 30°C at a rate of 40 mA/g. The first seven segments of discharge proceeded for one hour (40 mAh/g). The following five segments discharged for 2.5 hours (100 mAh/g) each and the final seven segments were discharged for 2.1 hours (84 mAh/g) each until a potential cutoff of 0.03 V. The cells were allowed to rest for 48 hours under open circuit voltage following each discharge segment. After 48 hours, the cell temperature was

decreased to 25 °C. The temperature was increased in steps of 2.5°C to a peak temperature of 35°C. At each step the temperature was held for 2 hours to allow for equilibration. Finally, the temperature was returned to 30°C for an additional 10 hours. A second order polynomial line was fit to the OCPs measured at 30°C before, during and after the temperature steps to normalize the OCP data. An example of a potential profile with temperature steps and corrected potential profile is shown in **Figure S1**. The five corrected temperature data points were linearly fit to calculate dE/dT all with R^2 values greater than 0.95. Entropic contributions to heat flow were calculated as the product of current (40 mA/g), temperature (30°C) and change in OCP with respect to temperature (dE/dT).

In the procedure above, OCP values were measured over the course of 68 hours after their discharge segment. However, 68 hours is not a sufficient length of time for total equilibration of Fe_3O_4 during lithiation. A previous report showed that OCPs for Fe_3O_4 required up to 500 hours to reach an apparent plateau.[11] Thus, the measured OCP values were extrapolated from 68 hours to 500 hours in order to estimate their equilibrium values. The extrapolated OCPs were then used to calculate polarization heating values during discharge. The polarization contribution was determined at each increment as the difference between loaded potential and OCP multiplied by the current.

2.3.3 Operando synchrotron-based X-ray microfluorescence (μ-XRF) mapping and X-ray absorption spectroscopy (XAS) measurements.

X-ray microfluorescence (μ-XRF) mapping and X-ray absorption spectroscopy (XAS) measurements of Li/Fe_3O_4 experimental cells were acquired at beamline 5-ID of the National

Synchrotron Light Source II (NSLS II) at Brookhaven National Laboratory. Kirkpatrick-Baez (KB) mirrors were used to create a focused spot of approximately 2 μm x 2 μm with energy tunable via a double crystal monochromator. The monochromator was calibrated using Fe metal foil and μ-XRF maps were collected at 7.2 keV to excite the Fe K-edge (7.112 keV). Samples were oriented approximately 45° relative to the incident beam and were rastered in the beam path using an XY-stage. X-ray fluorescence was detected using a 3-element Vortex ME3 silicon drift detector positioned at 45° relative to the sample. Data was collected over a sample area of 200 μm x 200 μm using a step size of 5 μm and an acquisition time of 0.2s. Data acquisition and visualization were performed using Python-based beamline software developed for NSLS-II Beamline 5-ID. μ-XRF maps were generated by fitting the fluorescence spectra using PyXRF Python-Based X-ray Fluorescence Analysis Package.[34] The integrated intensity of the Fe Kα1 fluorescence line at 6.4 eV was normalized by the incident beam energy for each image.

From the μ-XRF elemental maps, specific points were selected for XAS measurements were collected on specified points with 2 μm x 2 μm spatial resolution using fluorescence geometry at the Fe edge. Energy was scanned with a step size of 5 eV in the pre-edge region (-100 to -15 eV below the edge), while across the edge (-15 eV to 30 eV), the step size was 0.5 eV. In the post-edge region (30 to 350 eV above the edge) the step size was variable and gradually increased from 1 eV to 3.6 eV. XAS data were aligned and normalized using Athena software.[35] Linear combination fitting (LCF) of the x-ray absorption near edge structure (XANES) was performed using Athena software.[35] Three reference spectra were used for LCF: the pristine (undischarged) cell, the cell lithiated to 2.0 Li per mole of Fe_3O_4 ($Li_{2.0}Fe_3O_4$) and Fe^0 foil. Fits were performed on data 20 eV below to 40 eV above the edge energy (E_0). Average oxidation

state of Fe at various positions after lithiation was calculated using the sum of the fractions of each phase multiplied by their respective oxidation state.

Cells for the *operando* measurements were assembled using a working electrode (80 wt% Fe_3O_4, 20 wt% PVDF), polyethylene separator, and lithium metal anode. For each cell, an initial μ-XRF map was collected prior to lithiation and positions were specified for XAS measurements. The cells were discharged at a rates of C/10, C/2 or 2C to a cutoff potential of 0.1 V. XAS measurements were collected throughout discharge at selected points on the μ-XRF maps to track changes to the Fe edge during reduction. Post discharge, additional μ-XRF data were collected.

3. Results and Discussion

3.1 Isothermal Microcalorimetry (IMC)

Li/magnetite (Fe_3O_4) cells with crystallite sizes of 12 nm or 29 nm (determined by Rietveld refinement of XRD patterns, **Figure S2**) were discharged under a constant current while heat flow was simultaneously monitored using isothermal microcalorimetry (IMC). The cell potential and heat flow profiles for representative cells with 12 and 29 nm Fe_3O_4 during the first lithiation process are presented in **Figure 1**. To ensure the reproducibility of the IMC measurements, 3 cells with 12 nm Fe_3O_4 electrodes and 3 cells with 29 nm Fe_3O_4 electrodes were analyzed. Results for the replicate cells are included in the supplemental information file, Figures **S3** and **S4**. Similar heat flow profiles were also observed between replicate cells of each type, with integrated heat values of -4000 ± 100 J/g and 3690 ± 80 J/g for 12 nm electrodes and 29 nm electrodes, respectively, where the error is representative of one standard deviation from the mean. To interpret the heat flows determined via IMC, the lithiation mechanism of Fe_3O_4

must be considered. Previous studies have identified the mechanism as initiating with Li^+ insertion (equations 1 and 2) into the host spinel structure, followed by conversion to FeO and Fe^0 (equations 3 and 4).[4, 8]

(1) The first lithium equivalent intercalates into an interstitial octahedral (16c) site.

$$(\mathrm{Fe})_{8a}(\mathrm{Fe}_2)_{16d}\mathrm{O}_4 + \mathrm{Li}^+ + \mathrm{e}^- \rightarrow (\mathrm{LiFe})_{16c}(\mathrm{Fe}_2)_{16d}\mathrm{O}_4 \quad (1)$$

(2) The second lithium equivalent intercalates into the Fe_3O_4 lattice, displacing the Li^+ already situated in 16c sites and the two Li^+ are redistributed between 8a, 48f and 8b interstitial tetrahedral sites.

$$(\mathrm{LiFe})_{16c}(\mathrm{Fe}_2)_{16d}\mathrm{O}_4 + \mathrm{Li}^+ + \mathrm{e}^- \rightarrow (\mathrm{Li}_2)_{8a/48f/8b}(\mathrm{Fe}_3)_{16c/16d}\mathrm{O}_4 \quad (2)$$

(3) The third and fourth lithium equivalents result in the formation of a $Li_2O{\cdot}FeO$ and Fe^0 metal composite:

$$(\mathrm{Li}_2)_{8a/48f/8b}(\mathrm{Fe}_3)_{16c/16d}\mathrm{O}_4 + 2\mathrm{Li}^+ + 2\mathrm{e}^- \rightarrow 2\mathrm{Li}_2\mathrm{O} \cdot \mathrm{FeO} + \mathrm{Fe}^0 \quad (3)$$

(4) Reaction of the final four lithium equivalents produce iron metal and Li_2O:

$$2\mathrm{FeO} + 4\mathrm{Li}^+ + 4\mathrm{e}^- \rightarrow 2\mathrm{Li}_2\mathrm{O} + 2\mathrm{Fe}^0 \quad (4)$$

Thus, the overall lithiation reaction for Fe_3O_4 is (5):

$$Fe_3O_4 + 8Li^+ + 8e^- \rightarrow 3Fe^0 + 4Li_2O \quad (5)$$

On the basis of the overall reaction (equation 5), changes in enthalpy (ΔH_{rxn}), entropy (ΔS_{rxn}) and Gibbs free energy (ΔG_{rxn}) were estimated using standard heats of formation (H_f) and standard entropies (S_f) for $Fe_3O_{4\,(s)}$, $Fe_{(s)}$, $Li_{(s)}$ and $Li_2O_{(s)}$.[36] The overall reaction (5) predicts a release of 5,508 J per gram of for the full lithiation of Fe_3O_4 (**Table 1**). The total energy released from the lithiation of magnetite was determined by measuring total heat evolved (Q) with IMC and the electrical work (W). For both crystallite sizes the combined heat and work output exceeded the theoretical change in Gibbs free energy. Furthermore, the experimental cells exhibited capacities in excess of the theoretical 8 electron equivalents by 1.6 and 2.1 electron equivalents, for 12 and 29 nm samples, respectively. Thus, the extra released energy and delivered capacity suggest the occurrence of other heat-generating reduction processes in addition to the lithiation of Fe_3O_4.

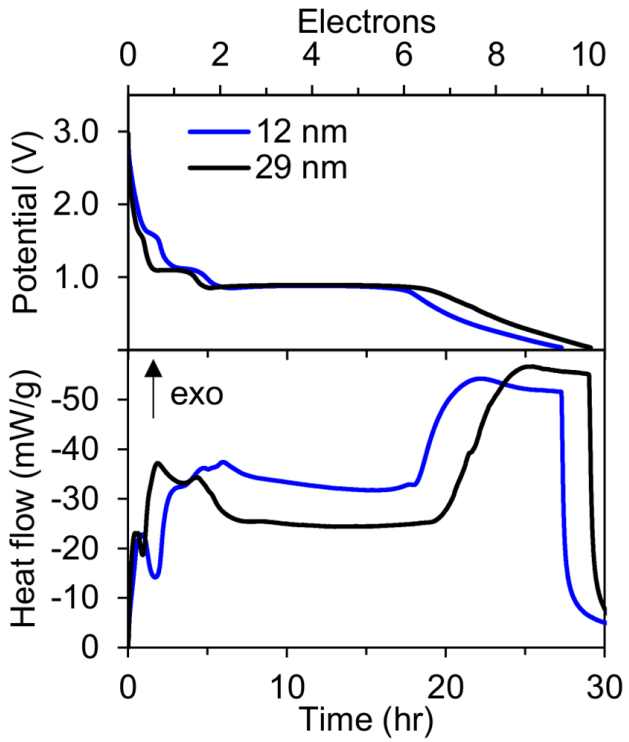

Figure 1. Potential(top) and heat flow(bottom) profiles for the lithiation of Fe_3O_4 under a current of 40 mA/g of Fe_3O_4 to a potential of 0.03 V. Heat flow is reported in mW per gram of Fe_3O_4 and negative values indicate heat leaving the cell (exothermic = "exo").

Theoretical

Capacity (mAh/g)	Capacity (Li equivalents)	ΔH_{rxn} (J/g)	$T\Delta S_{rxn}$ (J/g)	ΔG_{rxn} (J/g)= ΔH_{rxn}- $T\Delta S_{rxn}$
926	8.0	-5503	4.844	-5508

Measured

Crystallite size (nm)	Capacity (mAh/g)	Capacity (Li equivalents)	Q, Heat (J/g)	W, Work (J/g)	ΔH_T (J/g)= Q-W
12	1110	9.6	-4014	3066	-7080
29	1164	10.1	-3704	3220	-6924

Table 1. Theoretical capacity, enthalpy(ΔH_{rxn}), entropy (ΔS_{rxn}) and Gibbs free energy (ΔG_{rxn}) for the complete reaction of Fe_3O_4 and eight Li to form Fe^0 metal and Li_2O. Measured data shows the heat measured from IMC and electrochemical work for the lithiation of Fe_3O_4.

During the initial stages of lithiation, between 0 and 2 electron equivalents, the 12 nm Fe_3O_4 electrode operates at a higher potential than the 29 nm electrode with lower heat flow, indicative of reduced polarization. In this discharge region, two Li^+ ions insert into vacant interstitial sites within Fe_3O_4 while the average Fe oxidation state is reduced from 2.67 to 2, as represented by equations (1) and (2).[4] Smaller crystallites are less polarized during intercalation mechanisms due to shorter intracrystal diffusion distances.[6-8, 10, 37-40]

After the initial insertion process, the lithiation of Fe_3O_4 progresses to the conversion reactions of $Li_xFe_3O_4$ to $FeO{\cdot}Li_2O$ and Fe^0, occurring during the long voltage plateau at ca. 0.87 V.[4, 8] Along this plateau, the 29 nm electrode exhibited a 10-15 mV higher voltage (inset of **Figure 1**) and heat flows 8-10 mW/g lower than the 12 nm electrode. Thus, at this lithiation level the smaller crystallite material was more polarized, the inverse of the trend observed in the intercalation stage. Previous *operando* thermodynamic and x-ray absorption spectroscopic analyses have identified that parasitic reactions associated with SEI formation occur shortly after

two electron equivalents of reduction for Fe_3O_4.[32] Thus, the polarization after lithiation by >2.0 electron equivalents is influenced by SEI formation.

The measured heat flow reached a maximum at the end of discharge (beyond 6.0 e-) when the potential decreased from 0.87 to 0.03 V. Previous reports of the Fe_3O_4 lithiation mechanism indicate that the reduction product, Fe^0 metal, is present in this voltage region.[4, 8, 32] The 29 nm Fe_3O_4 electrode reached a greater peak heat flow, but maintained a higher potential during this voltage range compared to the 12 nm sample. With a higher operating voltage, the higher heat flow may not be attributed to greater polarization, but more likely to increased parasitic heat.

Total heat flow measured with IMC was interpreted with an energy balance for a battery to isolate the individual components that contribute to heat generation. The first law of thermodynamics states that the change in internal energy (ΔU) of a system is equal to heat ($\dot{Q}$) and work ($\dot{W}$) released or absorbed by the system. For a constant volume system, such as the sealed coin cells used in this study, the change in internal energy is equivalent to the change in enthalpy (ΔH_{tot}).

$$\frac{\Delta U}{dt} = \frac{\Delta H_{tot}}{dt} = \dot{Q} - \dot{W} \tag{6}$$

The total change in enthalpy for the general energy balance of batteries includes contributions from enthalpies of reactions, enthalpies of mixing, phase changes and heat capacity.[41-42] For this study the enthalpies of mixing and phase changes are considered negligible and heat capacity is not involved since the experiments were performed isothermally. Derivation

of the energy balance is provided in the Supplemental Information and the energy balance for these experiments can be simplified to[26]:

$$\dot{Q} = I\left(E_{load} - E_{ocp}\right) + I\left(T\frac{dE_{ocp}}{dT}\right) + \dot{Q}_p \quad (7)$$

The total heat ($\dot{Q}$) is comprised of contributions from three main components: (1) polarization heating, (2) entropic changes, and (3) parasitic reactions. Polarization heating occurs due to the Joule heating created from passing a current through the internal battery resistance. Polarization is observed by the cell overpotential (E_{load} - E_{ocp}) where ohmic losses, charge-transfer overpotential, and mass-transfer limitations influence cell resistances. Reactions at the anode and cathode cause entropy changes that result in entropic heating $I(T\frac{dE_{ocp}}{dT})$. The final term, $\dot{Q}_p$, is heat flow from non-faradaic reactions typically a result of SEI formation or other parasitic reactions. Contributions from these three components are considered in analysis of the results.

3.2 Polarization and entropic heating

In order to interpret the differences in IMC heat flow between the 12 nm and 29 nm electrodes, the polarization and entropic heating contributions to total heat flow were determined. Polarization, or resistive joule heating, was calculated by multiplying the discharge current by the difference in the loaded and open-circuit potentials throughout the first lithiation (**Figure 2**). The polarization contribution calculation captures all sources of polarization in the system, including charge transfer resistances (including charge transfer through the formed SEI and other interfaces), mass transfer limitations (including concentration overpotential which develops as a

result of electrode tortuosity), solid phase diffusion limitations, and ohmic resistances in the cell. During the initial 2 electron equivalents of lithiation, the 29 nm electrode exhibited greater polarization, while after the intercalation stage (> 2 electron equivalents), the 12 nm Fe_3O_4 displayed increased polarization. This result is consistent with the heat flows determined from IMC. Notably, the heat flow due to polarization was significant (12-35 mW/g) despite utilizing a slow discharge rate (C/25). Polarization can be minimized at slower rates, but electrochemical studies have shown that conversion electrodes have an inherent overpotential (~0.65 V) even at low current density.[43-44] The large inherent overpotentials in conversion electrodes have been attributed to the sluggish rearrangement of Li^+ and transition metal ions during phase transformations.[45]

The most striking result of the calculated polarization contributions to heat flow is the apparent reversal in the relationship between polarization and crystallite size at approximately 2 electron equivalents of reduction. The crystallite size material (12 nm) mitigated polarization during the first two electron transfers when the reduction mechanism consists of Li^+ intercalation into the interstitial sites of the parent Fe_3O_4 inverse spinel structure. Beyond 2 electron equivalents, when conversion to FeO and Fe^0 occurs, the smaller crystallites (12 nm) resulted in increased polarization. This finding is further explored in the next section on the non-faradaic contributions to generated heat flow.

Entropic changes during the lithiation were calculated using the temperature dependence of the open circuit voltage (**Figure 2c**). The entropic term was calculated using the formula I*T*dE/dT, where I is discharge current, T is discharge temperature (303.15 K) and dE/dT is the linear change in OCV with respect to temperature. The calculated entropic term is the partial derivative of the total entropy of the Li/Fe_3O_4 system with respect to the number of coulombs

transferred.[46] Negative entropy values indicate that passage of charge decreases the system disorder. Interestingly, the 12 nm Fe_3O_4 showed more negative entropic changes during the first lithiation relative to the 29 nm Fe_3O_4.

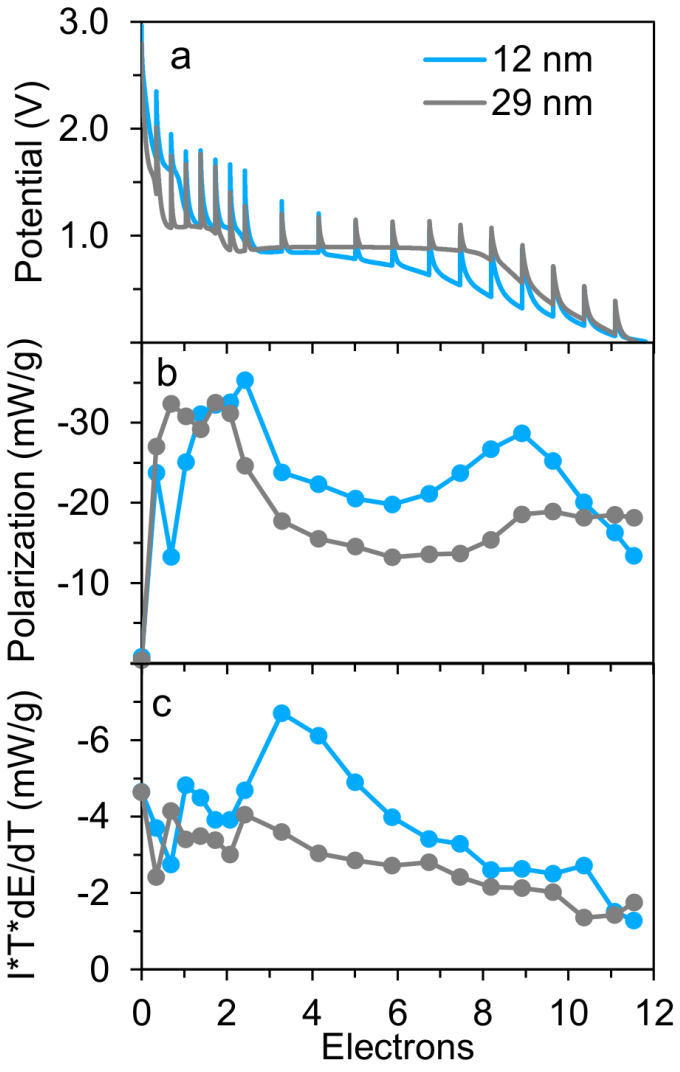

Figure 2. (a) Potential profile during discharge with intermittent rest steps. Upticks in potential represent positions where the applied current was removed and the cell potential recovered during the rest period. (b) Polarization and (c) entropic heating during the first lithiation of Fe_3O_4. Data for 12 nm Fe_3O_4 was adapted from [32].

3.3 Parasitic Reactions

The third contribution to heat flow within a battery is the generation of parasitic heat. Generated parasitic heat is visualized in **Figure 3** by comparing the summed contributions of polarization and entropic heating with the IMC heat flow profile. During the intercalation stage of reduction (0-2 e-) the IMC heat flow was matched by the predictions based on polarization and entropy contributions. The predicted and experimentally observed heat flows began to deviate at the start of the ~0.87 V plateau and continued to diverge until the potential limit of 0.03 V. The differences between the total heat flow (IMC) and the contributions from polarization and entropic heating were attributed to parasitic side reactions including those associated with the formation of the SEI layer on the Fe_3O_4 active material surfaces. A previous report used this methodology in conjunction with *operando* XAS to demonstrate that the onset of SEI formation occurs after two electron equivalents when the cell potential was ~0.87 V where discharge continues with no change in the oxidation state of the iron.[32] Notably, previous investigations report that the SEI forms at ca. 0.8 V vs. Li/Li^+, in good agreement with this observation.[13-14, 47-49] The differences between observed total heat flow by IMC and the sum of entropic and polarization contributions continued to increase during the region of voltage decay after 6 electron equivalents of reduction. Reports of other metal oxide conversion electrodes have claimed that fully reduced metal nanoparticles catalyze SEI reactions at potentials below 0.8 V.[17, 50-53] The increase in parasitic heat flow in this stage support the possibility of further electrolyte decomposition through the interaction with Fe^0 metal nanomaterials.

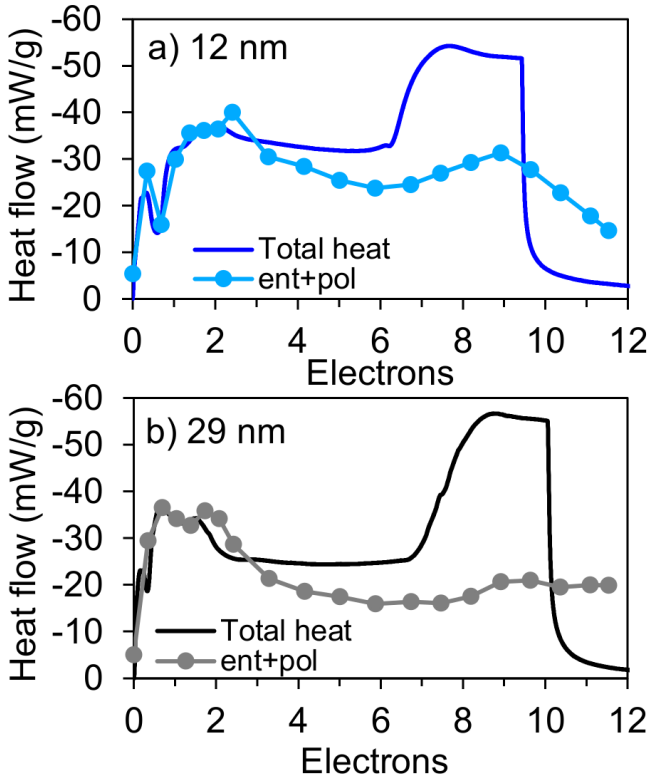

Figure 3. Polarization and entropic heating contributions were summed ("ent+pol") and compared to the total heat flow measured by IMC. Comparisons for Fe_3O_4 crystallite sizes of 12 nm (a) and 29 nm (b).

The heat generated from parasitic side reactions was quantified by integrating the area between IMC total heat flow and the predicted heat flows from polarization and entropic heating contributions (**Figure S5**). The 29 nm sample exhibited greater total parasitic heat (-1346 J/g) than the 12 nm Fe_3O_4 (-1155 J/g). The generated heat can be separated into three segments according to the lithiation mechanism of Fe_3O_4 (**Figure S5**). The first segment is the first two electrons of reduction when the mechanism is Li^+ intercalation and there is very little parasitic heat flow. The second segment is the long voltage plateau at ca. 0.8 V where the 29 nm Fe_3O_4

produced 43% more parasitic heat than 12 nm Fe_3O_4. (**Table S1**). The final segment is the region of voltage decay from 0.8 to 0.03 V where the 29 nm Fe_3O_4 produced 48% more parasitic heat. BET surface area of the 12 nm Fe_3O_4 (100 m^2/g) was significantly higher than that of the 29 nm Fe_3O_4 powder (26 m^2/g), indicating that the surface area of the primary crystallites alone does not correspond to the level of electrolyte reduction during SEI formation. The role of agglomeration of the 12 nm and 29 nm Fe_3O_4 particles was further investigated, and is discussed in subsequent sections, to further explore the observed results.

Crystallite Size (nm)	Total heat IMC (J/g)	Total heat predicted (J/g)	Parasitic Heat (J/g)
12	-4014	-2859	-1155
29	-3704	-2358	-1346

Table 2. Total heat measured from IMC, predicted total heat from entropic changes and polarization, and calculated parasitic heat (reflecting the difference in IMC and predicted heat) for 12 nm and 29 nm Fe_3O_4 electrodes.

3.4 SEM images of prepared electrodes

The results of the thermodynamic analysis of 12 nm vs. 29 nm electrodes were further explored by assessing the possible role of agglomeration on parasitic reactions. SEM images of electrodes prepared with 80 wt% Fe_3O_4 and 20 wt% PVDF show that 12 nm Fe_3O_4 formed dense agglomerates with an averaged diameter of several microns. (**Figure 4(a,b)**). In contrast,

electrodes prepared with 29 nm Fe_3O_4 exhibited fewer large agglomerates, suggesting that the Fe_3O_4 particles are more dispersed within the polymer matrix. A magnified view of the electrode containing 29 nm Fe_3O_4 particles indicates that it is more porous compared to that of the 12 nm crystallites. (**Figure 4(c,d)**). These findings are not unexpected, as smaller crystallites have high surface energy resulting from large surface area to volume ratios. These results suggest that the denser, more tightly packed agglomerates of 12 nm Fe_3O_4 could restrict electrolyte access, thus limiting the amount of solid electrolyte interphase that can form during electrolyte reaction.

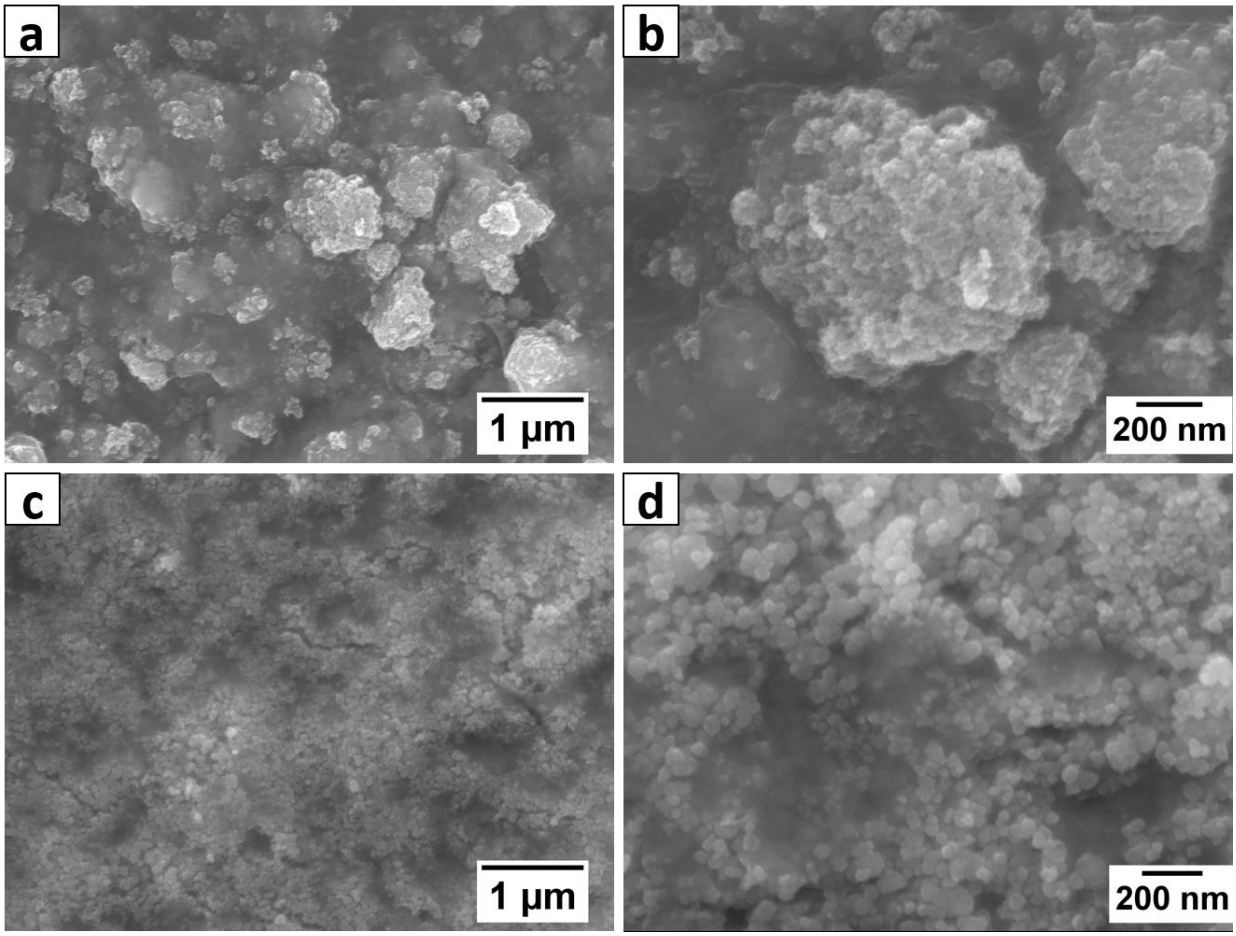

Figure 4. Scanning electron microscope (SEM) images of coatings prepared with 80 wt% Fe_3O_4 and 20 wt% PVDF. Coatings with 12 nm Fe_3O_4 are shown in (a, b) while coatings with 29 nm Fe_3O_4 are shown in (c, d).

3.5 Submicron Resolution X-ray Spectroscopy

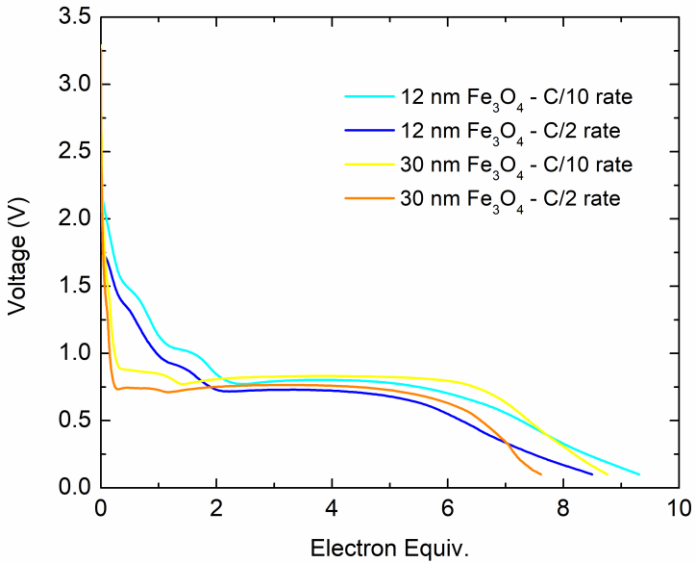

Figure 5. Comparison of electrochemistry data for operando Li/Fe_3O_4 cells having either 80% 12 nm Fe_3O_4, 20% PVDF or 80% 12 nm Fe_3O_4, 20% PVDF. Electrolyte is 1 M $LiPF_6$ 30:70 EC:DMC. Cells with were discharged at both C/10 and C/2 rates.

In order to further interrogate the role of agglomeration on the resulting electrochemistry of the 12 nm and 29 nm Fe_3O_4 electrodes, *operando* x-ray fluorescence elemental mapping in combination with spatially resolved X-ray absorption near edge spectroscopy (XANES) measurements were performed on Li/Fe_3O_4 batteries. This technique enabled probing of oxidation state evolution as a function of spatial position on the Fe_3O_4 aggregates. For both 12 nm and 29 nm Fe_3O_4 electrodes, *operando* measurements were performed at both C/10 and C/2 discharge rates. **Figure 5** shows an overlay of the voltage profiles for the four operando cells during lithiation to 0.01 V vs. Li/Li^+. In good agreement with the data collected on coin cell based batteries at C/24 rate (**Figure 1**), 12 nm electrodes exhibited reduced polarization during

initial lithiation prior to 2 electron equivalents of reduction. Furthermore, when comparing the operando cells containing 12 nm or 29 nm electrodes for a given discharge rate (C/10 or C/2), the 29 nm electrodes had higher loaded voltage along the long voltage plateau from ca. 2 – 6 electron equivalents, indicating greater polarization of the 12 nm electrodes after initiation of SEI formation and the conversion reaction to Fe^0 metal.

For each of the four cells, prior to discharge a 200 x 200 µm Fe K-edge elemental map of the electrode was collected, focusing on a region of agglomerated crystallites. Post discharge, a fluorescence map of the same region was re-collected. Comparison of pre and post discharge maps for 12 nm – C/10, 12 nm – C/2, 29 nm – C/10, and 29 nm – C/2 operando cells are shown in supplementary figures **S8**, **S10**, **S12,** and **S13**, respectively. For 12 nm based electrodes, minimal movement (< 10 µm) of the electrodes was observed, though some apparent cracking of the larger agglomerates appears to have occurred during the discharge. For the 29 nm electrodes discharged at C/10 rate, significant differences in the morphology of the aggregates before and after discharge were observed, though only slight movement of the 29 nm electrode was observed under discharge at the higher C/2 rate.

The most notable difference between the fluorescence maps of the 12 nm vs. 29 nm electrodes is the variation in signal intensity of aggregated vs. unaggregated regions of the Fe_3O_4. For 12 nm electrodes, the fluorescence signal intensity varies by > 500% between aggregated and de-aggregated regions of the electrode, while for the 29 nm electrodes, this difference is only ca. 150 – 200 %. Thus, the fluorescence maps suggest that for 12 nm Fe_3O_4, the aggregates are considerably more dense and tightly packed compared to the aggregates of 29 nm Fe_3O_4. The fluorescence maps also suggest that for the 12 nm Fe_3O_4 electrodes, a greater percentage of Fe_3O_4 is contained in agglomerates. These findings are in good agreement with the SEM

images in Figure 4, which also indicate more significant agglomeration and higher agglomerate packing density for the 12 nm Fe_3O_4 electrodes.

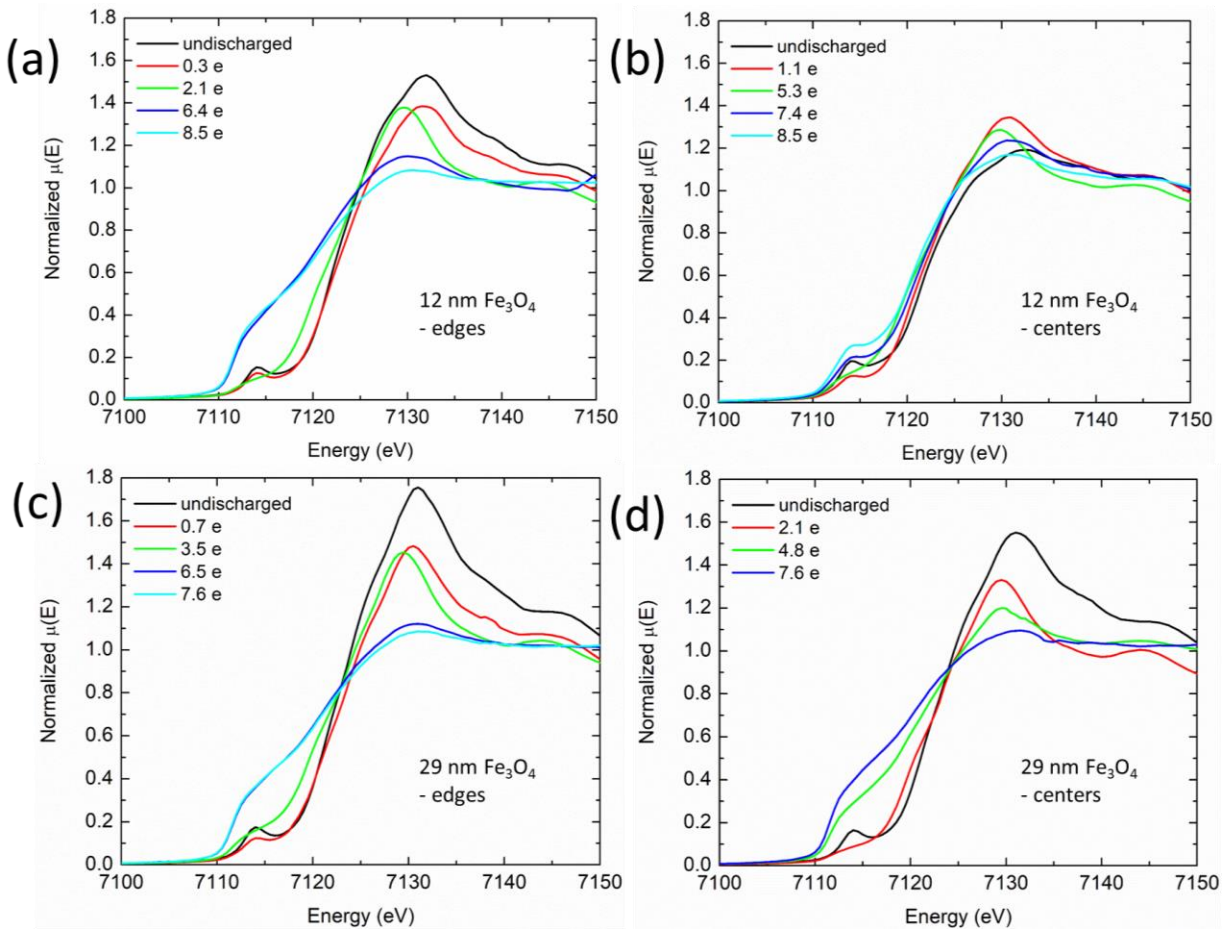

Figure 6. Operando XANES data for (a, b) 80% 12 nm Fe_3O_4, 20% PVDF electrodes and (c, d) 80% 29 nm Fe_3O_4, 20% PVDF electrodes discharged at a C/2 rate. XANES spectra were collected at regions alternating between the edges and centers of the Fe_3O_4 aggregates. Spectra from the edges of the aggregates are shown in (a, c), spectra from the center of the aggregates are shown in (b, d).

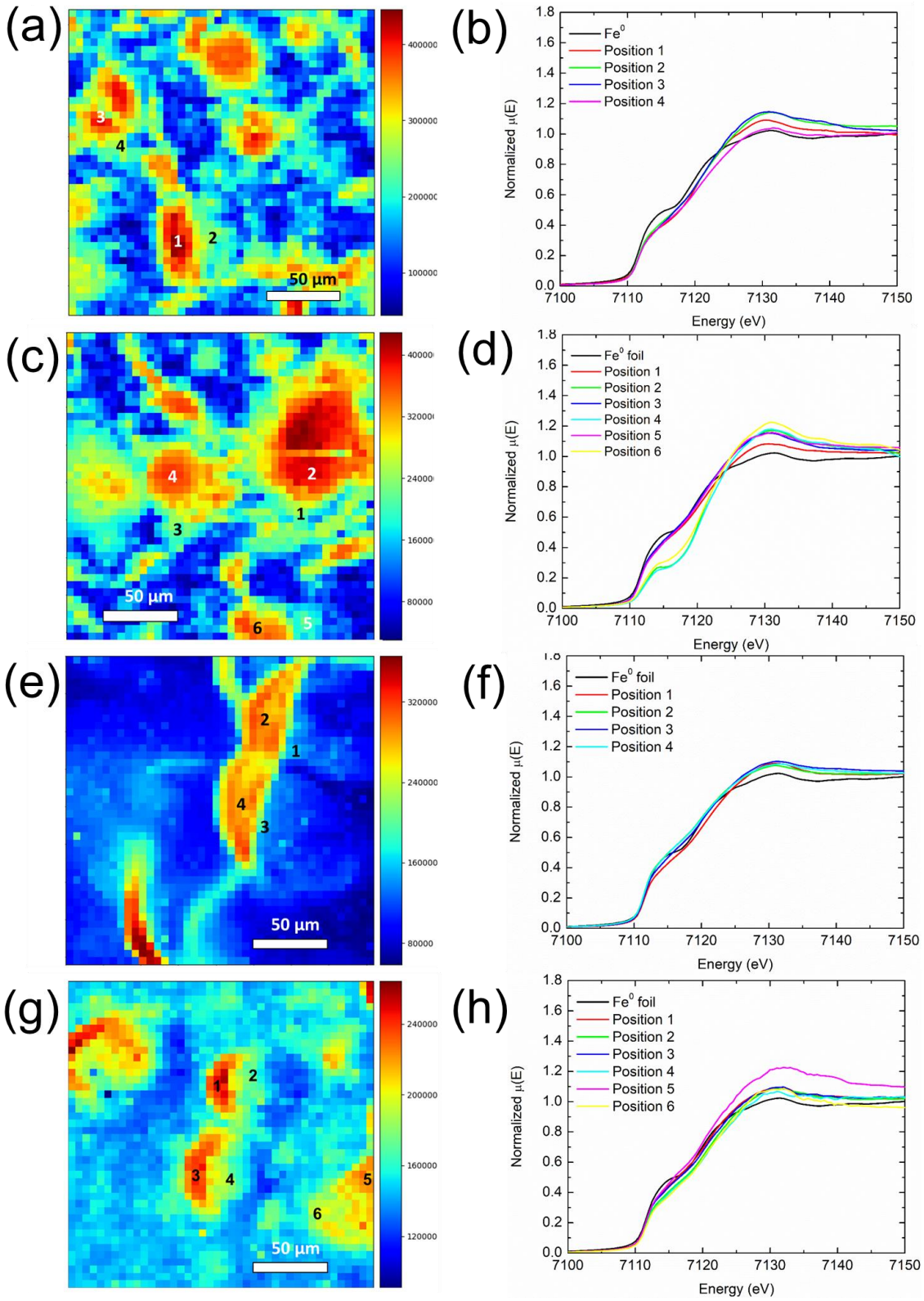
(a)
(b)
(c)
(d)
(e)
(f)
(g)
(h)
50 µm
Fe0
Fe0 foil
Position 1
Position 2
Position 3
Position 4
Position 5
Position 6
Normalized µ(E)
Energy (eV)

Figure 7. (a, c, e, g) In-situ XRF maps at collected on operando cells post discharge at an energy of 7200 eV. (b, d, f, h) XANES spectra collected at points specified on the corresponding XRF maps. (c, f, i, l). Data is shown for (a-d) 80% 12 nm Fe_3O_4, 20% PVDF electrodes and (e-f) 80% 29 nm Fe_3O_4, 20% PVDF electrodes discharged at (a,b,e,f) C/10 and (c,d,g,h) C/2 rates.

X-ray absorption near-edge structure (XANES) spectra were collected for each of the four cells throughout discharge, where measurements were collected at locations (spot size ca. 2 x 2 μm) alternating between the centers and edges of the Fe_3O_4 agglomerates to assess for differences in oxidation state evolution. *Operando* XANES data collected at C/2 rate are shown in **Figure 6** for 12 nm Fe_3O_4 (**Figure 6a, 6b**) and 29 nm Fe_3O_4 (**Figure 6c, 6d**) electrodes, while data for cells discharged at C/10 are shown in supplemental figures **S9 and S11**. For the 30 nm material, XANES spectra collected at both the edges (**Figure 6c**) and the centers of the agglomerates (**Figure 6d**) continually shift during discharge from an initial edge position of ca. 7125 eV in the undischarged state to lower energy, finally reaching a metallic-like edge energy of ca. 7112 eV by the end of discharge. The same uniform spectral shift is observed for the 12 nm electrode for data collected at the edges of agglomerates (**Figure 6a**). However, for spectra collected at the centers of the 12 nm aggregates (**Figure 6b**), the XANES spectra do not fully transition to a metallic oxidation state. Instead, at the end of discharge the spectra suggest that the active material has an intermediate or mixed oxidation state between that of Fe_3O_4 and Fe^0 metal. The inhomogeneity of oxidation state evolution between agglomerate edges and centers was not observed for the 12 nm electrode discharged at C/10 (**Figure S9**), indicating that Li^+ transport limitations are more apparent at faster discharge rates.

The differences in discharge homogeneity across agglomerates for 12 nm and 29 nm electrodes discharged at C/2 and C/10 rates were further probed by collecting XANES measurements at multiple agglomerate edge/center locations for each of the cells post discharge. **Figure 7** shows the specific locations on the XRF maps where the measurements were collected (denoted by numbers on the maps) along with the corresponding XANES spectra. Visual inspection of the data clearly indicate that for 12 nm – C/10, 30 nm – C/10, and 30 nm – C/2 cells, the spectra have similar edge position and spectral shape regardless of whether the data was collected at the center or the edge or an aggregate. In contrast, the 12 nm – C/2 cell exhibits consistent spectral differences dependent on the agglomerate edge or center position.

Linear combination fitting (LCF) of the post-discharge XANES data was used to estimate the phase compositions at each spatial position. The three reference spectra used for the LCF analysis were the undischarged electrode, the electrode at $Li_2Fe_3O_4$, and Fe metal. The undischarged and Fe metal references represent the initial and final states of the Fe center, while the partially lithiated $Li_2Fe_3O_4$ was used as a third, intermediate reference representing the lithiated Fe_3O_4 structure before the conversion reaction to Fe^0 and Li_2O. Analysis of the LCF indicate that the primary phase at aggregate edges and centers for the 12 nm – C/10, 30 nm – C/10, and 30 nm – C/2 cells, as well as at the edge positions of the 12 nm – C/2 cell, was Fe^0 metal (ca. 80%), with ca. 20% contribution of $Li_2Fe_3O_4$. However, aggregate centers of the 12 nm – C/2 cell contained a significantly higher percentage of $Li_2Fe_3O_4$, at ca. 50%. Average Fe oxidation state was calculated on the basis of the compositions determined by LCF (**Table 3**) and clearly show that the center of the 12 nm Fe_3O_4 aggregates, when discharged at the C/2 rate, have a higher oxidation state indicating only partial conversion to Fe^0 metal.

The spatially resolved XANES results unambiguously show that Li^+ transport limitations in agglomerates of 12 nm Fe_3O_4 are significant, resulting in discharge inhomogeneity in the edges vs. the centers of agglomerates. Reduced active material utilization for crystallites located in the centers of the agglomerates could be caused by restricted electrolyte access resulting from dense packing and low void space between the agglomerated 12 nmFe_3O_4 nanoparticles. In contrast, more loosely packed 30 nm crystallites of Fe_3O_4 exhibit homogeneous discharge due to reduced tortuosity of the electrolyte through the agglomerates. The significance of these findings as they relate to the thermodynamic analysis of 12 nm vs. 30 nm Fe_3O_4 is that the transport limitations and restricted electrolyte access in the 12 nm agglomerates could also limit the amount of SEI formation during discharge, resulting in a lower parasitic heat and for the 12 nm electrodes. Additionally, as SEI formation occurs, pathways for Li^+ transport through the densely packed agglomerates could be further restricted, resulting in greater polarization relative to the 29 nm electrodes.

Position # from XRF map	Average oxidation state from LCF fit			
	12 nm C/10	12 nm C/2	29 nm C/10	29 nm C/2
Position 1 (edge)	0.4 ± 0.1	0.2 ± 0.1	0.2 ± 0.1	0.2 ± 0.1
Position 2 (center)	0.4 ± 0.1	1.2 ± 0.1	0.1 ± 0.2	0.4 ± 0.1
Position 3 (edge)	0.5 ± 0.1	0.1 ± 0.1	0.2 ± 0.2	0.2 ± 0.1
Position 4 (center)	0.4 ± 0.1	1.2 ± 0.1	0.1 ± 0.2	0.4 ± 0.1
Position 5 (edge)	-	0.2 ± 0.1	-	0.4 ± 0.2
Position 6 (center)	-	1.1 ± 0.1	-	0.5 ± 0.1

Table 3. Calculated average oxidation states from LCF fitting results for spectra at positions identified on XRF maps in Figure 7.

3.6. *Heat flow during delithiation.*

IMC data including cell potential and heat flow profiles for representative cells with 12 and 29 nm Fe_3O_4 during the first delithiation is shown in **Figure 8**. Delivered capacity, heat evolved and work associated with the cells are tabulated in **Table 4.** Results for replicate cells measured under the same conditions are included in the supplemental information file, Figures **S3** and **S4**. Previous mechanistic studies of the delithiation of Fe_3O_4 indicate that the process proceeds via reconversion of Fe^0 nanoparticles and Li_2O domains to a disordered, highly nanocrystalline FeO-like structure:[4, 8]

$$Fe^0 + Li_2O \rightarrow FeO + 2Li^+ + 2e^- \quad (6)$$

The heat flow profiles for the 12 nm and 29 nm electrodes have the same general shape, with the heat evolution peaking at 3.0 V. However, the 29 nm electrodes deliver significantly greater capacity compared to the 12 nm electrodes, as well as greater heat flow associated with the higher degree of delithiation. The variation in delivered delithiation capacity and heat flow is caused by the different properties of the lithiated electrodes, which in turn impact the resulting delithiation process. These properties include differences in agglomeration of the active materials and differences in the quantity of formed SEI. Furthermore, it is also anticipated that the nature of the Fe^0 nanograins in the lithiated state also has an impact. In a previous report[8] , it was observed that the size and bond length disorder of Fe^0 nanograins in fully lithiated Fe_3O_4 is dependent on the Fe_3O_4 crystallite size, and that these differences impact the homogeneity of subsequent delithiated FeO phase.

It is notable that the 29 nm electrodes deliver significantly higher capacity during delithiation compared to the 12 nm electrodes. This finding provides additional evidence that significant transport limitations exist for the 12 nm electrodes after discharge, and is in good agreement with the spatially resolved XANES results.

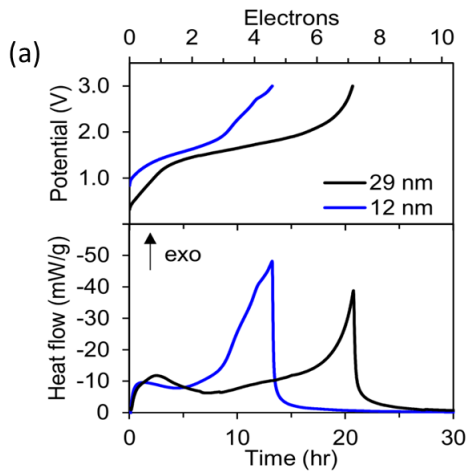

Figure 8. (a) Potential (top) and heat flow (bottom) profiles during the first delithiaton of Fe_3O_4. Representative data for 12 nm and 29 nm electrodes is shown.

Crystallite Size (nm)	Capacity (mAh/g)	Capacity (Li equivalents)	Total heat IMC (J/g)	Total Work (J/g)	ΔH = Q-W (J/g)
12	529	4.6	-815	-3504	2689
29	826	7.1	-968	-4916	3948

Table 4. Total heat and work measured during the first delithiation of Fe_3O_4 for representative cells with 12 nm and 29 nm electrodes.

Discussion

Electrochemical and thermodynamic analysis of Fe_3O_4 electrodes with 12 nm and 29 nm crystallite sizes indicate that: (1) cells with 12 nm Fe_3O_4 electrodes are less polarized than those with 29 nm material through the first 2 electron equivalents of reduction, (2) with the onset of SEI formation at ca. 0.8 V the relationship between polarization and crystallite size is reversed, with 29 nm samples being less polarized. These results were explored by assessing the role of agglomeration of the Fe_3O_4 nanoparticles by SEM, XRF mapping, and spatially resolved XANES. SEM results show that the 12 nm electrodes are more agglomerated than the 29 nm electrodes, and that the agglomerates of 12 nm Fe_3O_4 are more densely packed, and X-ray fluorescence maps of the aggregates within the electrodes during lithiation support this assertion. Furthermore, spatially resolved XANES measurements indicate more significant transport limitations for the 12 nm Fe_3O_4 electrodes.

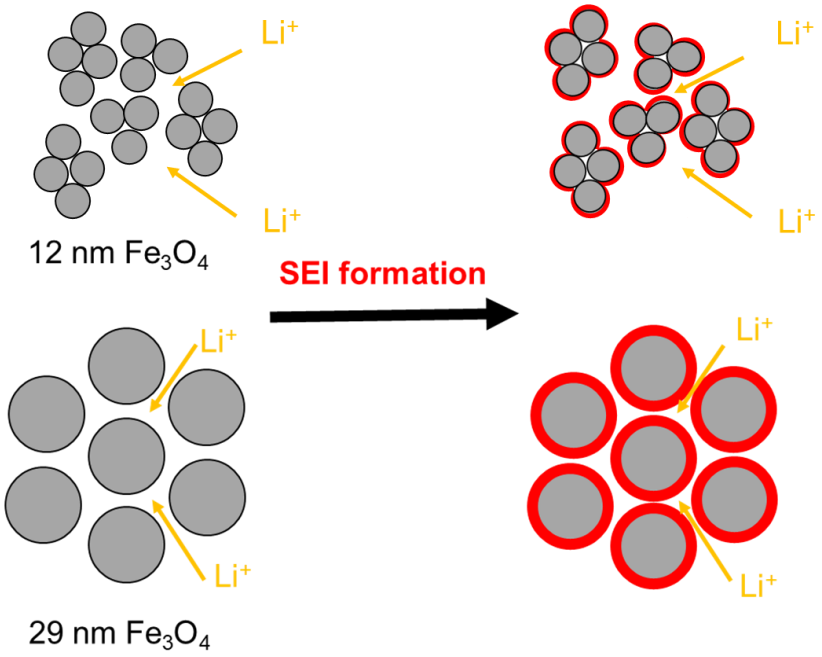

Figure 8. Schematic showing SEI formation on densely packed agglomerates of 12 nm Fe_3O_4 crystallites and crystallites of 30 nm Fe_3O_4.

The above results suggest that agglomeration of the 12 nm and 29 nm Fe_3O_4 particles plays a critical role in determining the amount of parasitic heat generated due to SEI formation, as well as the associated electrochemical behavior. This is illustrated schematically in **Figure 8**. While both 12 nm and 29 nm particles agglomerate, agglomerates of 12 nm Fe_3O_4 are significantly more closely packed, with less void space, relative to agglomerates of 29 nm Fe_3O_4. During initial reduction via intercalation through ca. 2 electron equivalents, which occurs prior to the onset of SEI, polarization is lower for the 12 nm material, primarily due to shorter material diffusion lengths vs. the 29 nm material. After the onset of SEI formation at ca. 0.8 V, the Li^+ diffusion channels in 12 nm Fe_3O_4 are significantly constricted. In contrast, for more loosely packed 29 nm crystallites, electrolyte access to the core of the agglomerates is not significantly reduced after SEI formation occurs. As a result, the Li^+ diffusion now more facile in the 29 nm electrodes than those with the 12 nm material. Furthermore, the amount of SEI formation in the 12 nm densely packed agglomerates is concentrated on the exterior of the agglomerates rather than the surface of each crystallite, resulting in a lower amount of parasitic heat generated relative to the 29 nm electrodes and consistent with the lower total discharge capacity. The assertion that agglomeration of Fe_3O_4 can limit the amount of SEI formation due to restricted electrolyte access has been previously reported in investigations of dispersed vs. agglomerated Fe_3O_4[15] as well as self-assembled Fe_3O_4 nanoparticle clusters,[18] supporting the proposed mechanism described above. While the transport limitations associated with the SEI formation are anticipated to contribute to capacity loss in the electrodes over extended cycling, it is noted that capacity fade in Fe_3O_4 is further complicated by additional factors, including (1) the loss of electrical contact between active material particles during volume expansion / contraction during

cycling[54], and (2) the size, disorder, and homogeneity of Fe^0 and FeO phases in lithiated and delithiated states respectfully, which impact the reversibility of the conversion reaction.[8] These factors also must be considered when assessing the cycling behavior of the Fe_3O_4 system.

4. Conclusion

The effects of both crystallite size and nanoparticle agglomeration on the heat generation was probed using isothermal microcalorimetry of cells containing electrodes of 12 nm or 29 nm Fe_3O_4. The heat evolved during lithation of the Fe_3O_4 was analyzed by comparing the total heat measured via IMC to the theoretical prediction based on heats of formation for the Faradaic reaction as well as cell polarization and entropic contributions. The results of the thermodynamic analysis were unanticipated, with the 29 nm Fe_3O_4 electrodes producing more parasitic heat than the 12 nm Fe_3O_4 electrodes (1346 J/g vs. 1155 J/g). The reduced parasitic heat flow for the smaller crystallite size material was further explored using scanning electron microscopy (SEM), XRF mapping, and spatially resolved XANES analyses. SEM images of the electrodes revealed more tightly packed agglomerates for the 12 nm material, with these results affirmed in the XRF maps. Furthermore *operando* spatially resolved XANES measurements showed higher transport limitations through the 12 nm Fe_3O_4 agglomerates. These results provide a mechanistic basis for the IMC results, where closely packed crystallites in agglomerates of the 12 nm material reduce electrolyte mobility and limit the amount of SEI formation, as well as corresponding parasitic heat generation, during the lithiation process.

Acknowledgements

This work was supported as part of the Center for Mesoscale Transport Properties, an Energy Frontier Research Center supported by the U.S. Department of Energy (DOE), Office of Science, Basic Energy Sciences, under award #DE-SC0012673.

M.M.H. and A. M. B. acknowledge the support of the National Science Foundation Graduate Research Fellowship under grant No. 1109408. Any opinions, findings, and conclusions or recommendations expressed in this material are those of the authors and do not necessarily reflect the views of the National Science Foundation.

This research used resources of beamline 5-ID, Submicron Resolution X-ray Spectroscopy (SRX) of the National Synchrotron Light Source II, a U.S. Department of Energy (DOE) Office of Science User Facility operated for the DOE Office of Science by Brookhaven National Laboratory under Contract No. DE-SC0012704.

References

1. Hussain, S. M.; Hess, K. L.; Gearhart, J. M.; Geiss, K. T.; Schlager, J. J., In Vitro Toxicity of Nanoparticles in Brl 3a Rat Liver Cells. *Toxicology in Vitro* **2005**, *19*, 975-983.

2. Bruck, A. M.; Cama, C. A.; Gannett, C. N.; Marschilok, A. C.; Takeuchi, E. S.; Takeuchi, K. J., Nanocrystalline Iron Oxide Based Electroactive Materials in Lithium Ion Batteries: The Critical Role of Crystallite Size, Morphology, and Electrode Heterostructure on Battery Relevant Electrochemistry. *Inorganic Chemistry Frontiers* **2016**, *3*, 26-40.

3. Fleet, M. E., The Structure of Magnetite: Symmetry of Cubic Spinels. *Journal of Solid State Chemistry* **1986**, *62*, 75-82.

4. Zhang, W.; Bock, D. C.; Pelliccione, C. J.; Li, Y.; Wu, L.; Zhu, Y.; Marschilok, A. C.; Takeuchi, E. S.; Takeuchi, K. J.; Wang, F., Insights into Ionic Transport and Structural Changes

in Magnetite During Multiple-Electron Transfer Reactions. *Advanced Energy Materials* **2016**, *6*, n/a.

5. Bruck, A. M.; Cama, C. A.; Gannett, C. N.; Marschilok, A. C.; Takeuchi, E. S.; Takeuchi, K. J., Nanocrystalline Iron Oxide Based Electroactive Materials in Lithium Ion Batteries: The Critical Role of Crystallite Size, Morphology, and Electrode Heterostructure on Battery Relevant Electrochemistry. *Inorg. Chem. Front.* **2016**, *3*, 26-40.

6. Zhu, S.; Marschilok, A. C.; Takeuchi, E. S.; Takeuchi, K. J., Crystallite Size Control and Resulting Electrochemistry of Magnetite, Fe3o4. *Electrochemical and Solid-State Letters* **2009**, *12*, A91-A94.

7. Zhu, S.; Marschilok, A. C.; Takeuchi, E. S.; Yee, G. T.; Wang, G.; Takeuchi, K. J., Nanocrystalline Magnetite: Synthetic Crystallite Size Control and Resulting Magnetic and Electrochemical Properties. *Journal of the Electrochemical Society* **2010**, *157*, A1158-A1163.

8. Bock, D. C., et al., Size Dependent Behavior of Fe3o4 Crystals During Electrochemical (De)Lithiation: An in Situ X-Ray Diffraction, Ex Situ X-Ray Absorption Spectroscopy, Transmission Electron Microscopy and Theoretical Investigation. *Physical Chemistry Chemical Physics* **2017**, *19*, 20867-20880.

9. Kang, E.; Jung, Y. S.; Cavanagh, A. S.; Kim, G.-H.; George, S. M.; Dillon, A. C.; Kim, J. K.; Lee, J., Fe3o4 Nanoparticles Confined in Mesocellular Carbon Foam for High Performance Anode Materials for Lithium-Ion Batteries. *Advanced Functional Materials* **2011**, *21*, 2430-2438.

10. Bock, D. C.; Kirshenbaum, K. C.; Wang, J.; Zhang, W.; Wang, F.; Wang, J.; Marschilok, A. C.; Takeuchi, K. J.; Takeuchi, E. S., 2d Cross Sectional Analysis and Associated

Electrochemistry of Composite Electrodes Containing Dispersed Agglomerates of Nanocrystalline Magnetite, Fe3o4. *ACS Applied Materials & Interfaces* **2015**, *7*, 13457-13466.

11. Knehr, K. W.; Brady, N. W.; Cama, C. A.; Bock, D. C.; Lin, Z.; Lininger, C. N.; Marschilok, A. C.; Takeuchi, K. J.; Takeuchi, E. S.; West, A. C., Modeling the Mesoscale Transport of Lithium-Magnetite Electrodes Using Insight from Discharge and Voltage Recovery Experiments. *Journal of the Electrochemical Society* **2015**, *162*, A2817-A2826.

12. Knehr, K. W.; Brady, N. W.; Lininger, C. N.; Cama, C. A.; Bock, D. C.; Lin, Z.; Marschilok, A. C.; Takeuchi, K. J.; Takeuchi, E. S.; West, A. C., Mesoscale Transport in Magnetite Electrodes for Lithium-Ion Batteries. *ECS Transactions* **2015**, *69*, 7-19.

13. Bock, D. C.; Waller, G. H.; Mansour, A. N.; Marschilok, A. C.; Takeuchi, K. J.; Takeuchi, E. S., Investigation of Solid Electrolyte Interphase Layer Formation and Electrochemical Reversibility of Magnetite, Fe3o4, Electrodes: A Combined X-Ray Absorption Spectroscopy and X-Ray Photoelectron Spectroscopy Study. *The Journal of Physical Chemistry C* **2018**, *122*, 14257-14271.

14. Bock, D. C.; Marschilok, A. C.; Takeuchi, K. J.; Takeuchi, E. S., Deliberate Modification of the Solid Electrolyte Interphase (Sei) During Lithiation of Magnetite, Fe3o4: Impact on Electrochemistry. *Chemical Communications* **2017**, *53*, 13145-13148.

15. Bock, D. C., et al., Dispersion of Iron Oxide, Fe3o4, Nanomaterials in Composite Electrodes: Impact on Functional Electrochemistry. *ACS Applied Materials and Interfaces* **2016**, *8*, 11418 - 11430.

16. Sina, M.; Thorpe, R.; Rangan, S.; Pereira, N.; Bartynski, R. A.; Amatucci, G. G.; Cosandey, F., Investigation of Sei Layer Formation in Conversion Iron Fluoride Cathodes by Combined Stem/Eels and Xps. *Journal of Physical Chemistry C* **2015**, *119*, 9762-9773.

17. Gmitter, A. J.; Badway, F.; Rangan, S.; Bartynski, R. A.; Halajko, A.; Pereira, N.; Amatucci, G. G., Formation, Dynamics, and Implication of Solid Electrolyte Interphase in High Voltage Reversible Conversion Fluoride Nanocomposites. *J. Mater. Chem.* **2010**, *20*, 4149-4161.

18. Lee, S. H., et al., Self-Assembled Fe3o4 Nanoparticle Clusters as High-Performance Anodes for Lithium Ion Batteries Via Geometric Confinement. *Nano Letters* **2013**, *13*, 4249-4256.

19. Zhang, W. M.; Wu, X. L.; Hu, J. S.; Guo, Y. G.; Wan, L. J., Carbon Coated Fe3o4 Nanospindles as a Superior Anode Material for Lithium-Ion Batteries. *Advanced Functional Materials* **2008**, *18*, 3941-3946.

20. An, S. J.; Li, J.; Daniel, C.; Mohanty, D.; Nagpure, S.; Wood, D. L., The State of Understanding of the Lithium-Ion-Battery Graphite Solid Electrolyte Interphase (Sei) and Its Relationship to Formation Cycling. *Carbon* **2016**, *105*, 52-76.

21. Verma, P.; Maire, P.; Novák, P., A Review of the Features and Analyses of the Solid Electrolyte Interphase in Li-Ion Batteries. *Electrochimica Acta* **2010**, *55*, 6332-6341.

22. Aurbach, D.; Markovsky, B.; Shechter, A.; Ein-Eli, Y.; Cohen, H., A Comparative Study of Synthetic Graphite and Li Electrodes in Electrolyte Solutions Based on Ethylene Carbonate-Dimethyl Carbonate Mixtures. *Journal of the Electrochemical Society* **1996**, *143*, 3809-3820.

23. Andersson, A. M.; Edström, K., Chemical Composition and Morphology of the Elevated Temperature Sei on Graphite. *Journal of the Electrochemical Society* **2001**, *148*, A1100-A1109.

24. Li, J.; Downie, L. E.; Ma, L.; Qiu, W.; Dahn, J. R., Study of the Failure Mechanisms of Lini0.8mn0.1co0.1o2 Cathode Material for Lithium Ion Batteries. *Journal of the Electrochemical Society* **2015**, *162*, A1401-A1408.

25. Downie, L. E.; Dahn, J. R., Determination of the Voltage Dependence of Parasitic Heat Flow in Lithium Ion Cells Using Isothermal Microcalorimetry. *Journal of the Electrochemical Society* **2014**, *161*, A1782-A1787, 6 pp.

26. Downie, L. E.; Hyatt, S. R.; Dahn, J. R., The Impact of Electrolyte Composition on Parasitic Reactions in Lithium Ion Cells Charged to 4.7 V Determined Using Isothermal Microcalorimetry. *Journal of the Electrochemical Society* **2016**, *163*, A35-A42.

27. Downie, L. E.; Hyatt, S. R.; Wright, A. T. B.; Dahn, J. R., Determination of the Time Dependent Parasitic Heat Flow in Lithium Ion Cells Using Isothermal Microcalorimetry. *J. Phys. Chem. C* **2014**, *118*, 29533-29541.

28. Glazier, S. L.; Downie, L. E.; Xia, J.; Louli, A. J.; Dahn, J. R., Effects of Fluorinated Carbonate Solvent Blends on High Voltage Parasitic Reactions in Lithium Ion Cells Using Ocv Isothermal Microcalorimetry. *Journal of the Electrochemical Society* **2016**, *163*, A2131-A2138.

29. Downie, L. E.; Nelson, K. J.; Petibon, R.; Chevrier, V. L.; Dahn, J. R., The Impact of Electrolyte Additives Determined Using Isothermal Microcalorimetry. *ECS Electrochemistry Letters* **2013**, *2*, A106-A109.

30. Hall, D. S.; Glazier, S. L.; Dahn, J. R., Isothermal Microcalorimetry as a Tool to Study Solid-Electrolyte Interphase Formation in Lithium-Ion Cells. *Phys. Chem. Chem. Phys.* **2016**, *18*, 11383-11390.

31. Hall, D. S., et al., Surface-Electrolyte Interphase Formation in Lithium-Ion Cells Containing Pyridine Adduct Additives. *Journal of the Electrochemical Society* **2016**, *163*, A773-A780.

32. Huie, M. M.; Bock, D. C.; Wang, L.; Marschilok, A. C.; Takeuchi, K. J.; Takeuchi, E. S., Lithiation of Magnetite (Fe3o4): Analysis Using Isothermal Microcalorimetry and Operando X-Ray Absorption Spectroscopy. *The Journal of Physical Chemistry C* **2018**, *122*, 10316-10326.

33. Martinez-Mera, I.; Espinosa-Pesqueira, M. E.; Perez-Hernandez, R.; Arenas-Alatorre, J., Synthesis of Magnetite (Fe3o4) Nanoparticles without Surfactants at Room Temperature. *Materials Letters* **2007**, *61*, 4447-4451.

34. Li, L.; Yan, H.; Xu, W.; Yu, D. T.; Heroux, A.; Lee, W. K.; Campbell, S. I.; Chu, Y. S., Pyxrf: Python-Based X-Ray Fluorescence Analysis Package. In *X-Ray Nanoimaging: Instruments and Methods Iii*, Lai, B.; Somogyi, A., Eds. 2017; Vol. 10389.

35. Ravel, B.; Newville, M., Athena, Artemis, Hephaestus: Data Analysis for X-Ray Absorption Spectroscopy Using Ifeffit. *Journal of Synchrotron Radiation* **2005**, *12*, 537-541.

36. Chase, M. W., Jr., *J. Phys. Chem. Ref. Data* **1998**, 1-1951.

37. Komaba, S.; Mikumo, T.; Ogata, A., Electrochemical Activity of Nanocrystalline Fe3o4 in Aprotic Li and Na Salt Electrolytes. *Electrochemistry Communications* **2008**, *10*, 1276-1279.

38. Komaba, S.; Mikumo, T.; Yabuuchi, N.; Ogata, A.; Yoshida, H.; Yamada, Y., Electrochemical Insertion of Li and Na Ions into Nanocrystalline Fe3o4 and A-Fe2o3 for Rechargeable Batteries. *Journal of the Electrochemical Society* **2010**, *157*, A60-A65.

39. Menard, M. C.; Marschilok, A. C.; Takeuchi, K. J.; Takeuchi, E. S., Variation in the Iron Oxidation States of Magnetite Nanocrystals as a Function of Crystallite Size: The Impact on Electrochemical Capacity. *Electrochimica Acta* **2013**, *94*, 320-326.

40. Menard, M. C.; Takeuchi, K. J.; Marschilok, A. C.; Takeuchi, E. S., Electrochemical Discharge of Nanocrystalline Magnetite: Structure Analysis Using X-Ray Diffraction and X-Ray Absorption Spectroscopy. *Phys. Chem. Chem. Phys.* **2013**, *15*, 18539-18548.

41. Bernardi, D.; Pawlikowski, E.; Newman, J., A General Energy Balance for Battery Systems. *Journal of the Electrochemical Society* **1985**, *132*, 5-12.

42. Rao, L.; Newman, J., Heat-Generation Rate and General Energy Balance for Insertion Battery Systems. *Journal of the Electrochemical Society* **1997**, *144*, 2697-2704.

43. Kraytsberg, A.; Ein-Eli, Y., A Critical Review-Promises and Barriers of Conversion Electrodes for Li-Ion Batteries. *Journal of Solid State Electrochemistry* **2017**, Ahead of Print.

44. Taberna, P. L.; Mitra, S.; Poizot, P.; Simon, P.; Tarascon, J. M., High Rate Capabilities Fe3o4-Based Cu Nano-Architectured Electrodes for Lithium-Ion Battery Applications. *Nature Materials* **2006**, *5*, 567-573.

45. Yu, H. C.; Ling, C.; Bhattacharya, J.; Thomas, J. C.; Thornton, K.; Van der Ven, A., Designing the Next Generation High Capacity Battery Electrodes. *Energy & Environmental Science* **2014**, *7*, 1760-1768.

46. Thomas, K. E.; Bogatu, C.; Newman, J., Measurement of the Entropy of Reaction as a Function of State of Charge in Doped and Undoped Lithium Manganese Oxide. *Journal of the Electrochemical Society* **2001**, *148*, A570-A575.

47. Su, L.; Zhong, Y.; Zhou, Z., Role of Transition Metal Nanoparticles in the Extra Lithium Storage Capacity of Transition Metal Oxides: A Case Study of Hierarchical Core–Shell Fe3o4@C and Fe@C Microspheres. *Journal of Materials Chemistry A* **2013**, *1*, 15158-15166.

48. Ponrouch, A.; Taberna, P.-L.; Simon, P.; Palacín, M. R., On the Origin of the Extra Capacity at Low Potential in Materials for Li Batteries Reacting through Conversion Reaction. *Electrochimica Acta* **2012**, *61*, 13-18.

49. Laruelle, S.; Grugeon, S.; Poizot, P.; Dollé, M.; Dupont, L.; Tarascon, J.-M., On the Origin of the Extra Electrochemical Capacity Displayed by Mo/Li Cells at Low Potential. *Journal of the Electrochemical Society* **2002**, *149*, A627-A634.

50. Tian, N.; Hua, C. X.; Wang, Z. X.; Chen, L. Q., Reversible Reduction of Li2co3. *Journal of Materials Chemistry A* **2015**, *3*, 14173-14177.

51. Poizot, P.; Laruelle, S.; Grugeon, S.; Dupont, L.; Tarascon, J. M., Searching for New Anode Materials for the Li-Ion Technology: Time to Deviate from the Usual Path. *Journal of Power Sources* **2001**, *97-98*, 235-239.

52. Grugeon, S.; Laruelle, S.; Dupont, L.; Tarascon, J. M., An Update on the Reactivity of Nanoparticles Co-Based Compounds Towards Li. *Solid State Sciences* **2003**, *5*, 895-904.

53. Laruelle, S.; Grugeon, S.; Poizot, P.; Dolle, M.; Dupont, L.; Tarascon, J. M., On the Origin of the Extra Electrochemical Capacity Displayed by Mo/Li Cells at Low Potential. *Journal of the Electrochemical Society* **2002**, *149*, A627-A634.

54. Cabana, J.; Monconduit, L.; Larcher, D.; Palacín, M. R., Beyond Intercalation-Based Li-Ion Batteries: The State of the Art and Challenges of Electrode Materials Reacting through Conversion Reactions. *Advanced Materials* **2010**, *22*, E170-E192.